

AD717278

①

a  
report [REDACTED]  
from the Texas A&M  
RESEARCH FOUNDATION  
College Station, Texas  
[REDACTED]

✓ D C  
RECEIVED  
JAN 23 1960  
A

**BEST  
AVAILABLE COPY**

STUDIES IN ROCK FRACTURE

John Handin

Center for Tectonophysics  
Texas A&M University  
College Station, Texas

Contract No. DACA73-68-C-0004

WORK SPONSORED BY ADVANCED RESEARCH PROJECTS AGENCY

DEPARTMENT OF DEFENSE

ARPA Order No. 1074 Amendment 1

TWELFTH QUARTERLY TECHNICAL REPORT

Period covered: August 1, 1970 - October 31, 1970

November 15, 1970

Technical Monitor: R. W. Bruhn

Distribution of this document  
is unlimited

Prepared  
for

DEPARTMENT OF THE ARMY  
OMAHA DISTRICT CORP OF ENGINEERS  
U.S. POST OFFICE AND COURTHOUSE  
OMAHA, NEBRASKA

## INTRODUCTION

This project, Studies in Rock Fracture, is an integrated program of theoretical, experimental, and field studies designed to improve our understanding of why, when, where, and how fracture occurs. It consists of three tasks: 1) Studies of Residual Strain (M. Friedman, J. M. Logan, D. W. Stearns), 2) Photomechanical Modeling (G. M. Sowers, D. W. Stearns), and 3) Fast Strain-Rate Testing (J. Handin, J. M. Logan). Task II was suspended on 1 May 1968, reinstated on 1 November 1969, and terminated on 31 October 1970. Our objectives, laboratory facilities, and experimental techniques are discussed in our First Quarterly Technical Report (15 February 1968). In this report we will summarize our progress during the twelfth quarter and plans for the thirteenth.

## TASK I

### Summary

1) In July, 1970, a major effort was directed toward the measurement of the in situ state of strain (stress) at an outcrop of Mesa Verde sandstone (Cretaceous), Site No. 1, on the N 45° W plunging nose of the Rangely Anticline, western Colorado. Participating were: Drs. C. B. Raleigh and R. V. de la Cruz of the U. S. Geological Survey, National Center for Earthquake Research, Menlo Park, California, using the CSIR "doorstopper" gage and the borehole deformation three-component gage of the U. S. Bureau of Mines; Mr. R. A. Farrow and associates working under the direction of T. C. Nichols, Jr., Engineering Branch of the U. S. Geological Survey, Denver, Colorado, using the solid-inclusion borehole gage; and our own staff

/

consisting of Drs. J. Handin and D. W. Stearns, using foil-resistance gages, and A. Brown using photoelastic gages. With exception of a few of the photoelastic determinations, all measurements were made within a circle with a radius of about 2 m and within the same joint-bounded block. In addition, a specimen of the sandstone was studied in the laboratory by materials testing, optical, and X-ray diffraction techniques by Dr. M. Friedman and associates. Results for the strain-relief measurements are expressed as stresses by using a value of  $5 \times 10^4$  bars ( $8 \times 10^5$  psi) for Young's Modulus, as determined independently by the Menlo Park and Denver groups of the U. S. Geological Survey. Compressive stresses are counted positive.

Data from the six techniques show a strong correlation with respect to the direction of the maximum principal compressive in situ stress  $\sigma_1$  at Site No. 1. On the other hand, there is only fair agreement with respect to the corresponding magnitudes. The two-dimensional technique of the U. S. Bureau of Mines by the Menlo Park group yields the average  $\sigma_1$  trend of N 63° E and has an average magnitude of 5 bars. The "doorstopper" gage gives  $\sigma_1$  of 17 bars at N 89° E. Our photoelastic surface gages at seven stations (nine rosettes) indicate an average orientation for  $\sigma_1$  of N 77° E with a range of N 63° E to N 88° E and an average  $\sigma_1$  of 15 bars. Foil-resistance surface gages at three stations indicate  $\sigma_1$  at N 73° E, N 63° E and N 88° E with values of 25 bars, 13 bars, and 28 bars, respectively. With respect to the three-dimensional techniques, the U. S. Geological Survey group at Denver reports that  $\sigma_1$  plunges 3° to the N 41° E and has a mean magnitude of 2 bars. The X-ray technique yields an average  $\sigma_1$  that is horizontal and trends N 70° E, but that has a very high average magnitude of 200 bars. Actually the strains measured with the X-ray technique are comparable to those from the foil-resistance gages. The much higher stresses

result from the use of Young's Modulus for the {3254} direction in quartz, i.e.,  $9 \times 10^5$  bars versus the value of  $5 \times 10^4$  bars for the rock as a whole. Both the three-dimensional techniques show that  $\sigma_3$  is tensile and inclined at high angles to the bedding.

2) By point loading discs of the sandstone perpendicular to bedding we detected a strong trend for the rock to fracture along the directions N 30° W to N 50° W. This trend is at high angles to the in situ  $\sigma_1$ , and is subparallel to the anticlinal axis and to one of the major fracture (joint) sets in the outcrop (N 26° W). This fracture anisotropy cuts across the orientation of apparent long axes of the sand grains which tend to lie statistically between N 60° E and E-W (i.e., subparallel to the in situ  $\sigma_1$ ). The induced fractures do not follow the trend of N 70° E as would be predicted from superposition of the point load on the pre-stress.

3) Initial testing in our apparatus designed to create stable tensile fracturing by bending notched prisms of rock have been successful. The force-deflection curve for a specimen of Tennessee sandstone is typical of stable fracture. The area under this curve, determined with a polar planimeter, is the external energy needed to propagate a tensile fracture from the notch tip. This energy divided by twice the true area of the fracture surface yields the effective surface energy of the fracture,  $\gamma_{eff}$ . Our value for  $\gamma_{eff}$  agrees well with a previously published value determined with a different loading scheme. Using a refined estimate for the true area of the fracture surface, we obtain  $3.8 \times 10^4$  ergs/cm<sup>2</sup>. This is one to two orders of magnitude larger than surface energies for different cleavages in quartz single crystals.

4) The extension-fracture criterion for rupture in large grains of uncemented, two-dimensional aggregates is expanded to include three-dimensional grains which are also two orders of magnitude smaller. These smaller grains are spherical glass beads that are experimentally deformed under a variety of conditions. Results of these experiments indicate that the fracture criterion applies at different scales to grains of any brittle material.

Measurement of In Situ and Residual Strain, Site No. 1, Rangely Anticline

In July, 1970, three research groups measured the in situ state of strain (stress) at an outcrop of Mesa Verde sandstone (Cretaceous) on the N 45° W plunging nose of the Rangely Anticline, Rio Blanco County, Colorado. Participating were: (1) Drs. C. B. Raleigh and R. V. de la Cruz of the U. S. Geological Survey, National Center for Earthquake Research, Menlo Park, California, using the CSIR "doorstopper" gage and the three-component borehole deformation gage of the U. S. Bureau of Mines; (2) Mr. R. A. Farrow and associates working under the direction of T. C. Nichols, Jr., Engineering Branch, U. S. Geological Survey, Denver, using their solid-inclusion borehole gage; and (3) Drs. John Handin, D. W. Stearns, and A. Brown, Center for Tectonophysics, Texas A&M University, using foil-resistance and photoelastic gages. In addition, the residual state of strain was measured by X-ray diffractometry in the Fabrics Laboratory of the Center. The use of the five different strain-relief (overcoring) techniques plus the X-ray method probably makes this a unique study of the in situ and residual strains for a particular site.

Descriptions of each of these strain-relief techniques are beyond the scope of this report. The interested reader is referred to the following publications. The CSIR "doorstopper" rock-stress measuring equipment is most recently reviewed by Leeman (1970). A description of the U. S. Bureau of Mines three-component gage is given by Merrill (1967), and the general subject is reviewed by Obert (1966). Voight (1967) discusses the use of photoelastic gages. The techniques involving foil-resistance gages have been developed primarily by our Stearns and by Dr. E. G. Bombolakis of Boston College. Stearns's technique and the influence of atmospheric changes on the apparent rock strains will be described in a forthcoming Quarterly Technical Report. Finally, the solid-inclusion borehole probe which detects three-dimensional stress changes is described by Nichols and others (1968).

Site No. 1 on the N 45° W plunging nose of the Rangely Anticline is located in Sec. 10, R. 103 W., T. 2 N. The outcrop is a low-relief exposure of nearly flat lying, massive Mesa Verde sandstone (Cretaceous). Within 10 meters of all the in situ measurements is a nearly vertical "cliff" face and talus slope. The combined height of face and slope is about 10 meters. Major, extensive fractures (joints) are spaced about 2 m apart as viewed on the bedding plane, but less conspicuous fractures occur at closer intervals. In general the fractures are developed in several ordered sets of which the prominent ones are essentially vertical and have average strikes of E-W, N 26° W and N 44° E (Figure 1). This particular outcrop was chosen for study because (a) it provides a structurally interesting location on the Rangely Anticline, (b) it is accessible to vehicles and drilling rigs, (c) the relatively massive sandstone is not too highly fractured, and (d) the rock is a quartzose sandstone, and therefore, amenable to X-ray analysis.

The rock itself is a tan, well sorted, medium grained, friable sandstone with at least 25 to 30 percent porosity and probably high permeability. Its solid phases consist of about 80% quartz, 8% rock fragments, 5% feldspar, and 7% interstitial clay and limonite. Grains are cemented only at their contacts most of which are modified into either short-planar or concavo-convex types. A few of the grains show partial overgrowths of secondary silica. Most of the grains exhibit undulatory extinction, healed microfractures, or quartz deformation lamellae. In thin sections cut parallel to bedding about a third of the grains have an apparent long to short dimensional ratio of  $\geq 2:1$  as discussed later.

The directions and magnitudes of all in situ and residual strains (stresses) are listed in Table 1. Magnitudes are expressed as stresses, compressions positive, to facilitate comparisons, particularly between the strain-relief and the X-ray techniques. Techniques Nos. 1 through 5 (Table 1) involve strain relief by overcoring and thus they measure the total in situ state of stress in the rock due to the superposition of presently applied loads on the paleo-prestresses (the residual stresses). The X-ray method, on the other hand, detects only the residual stresses, i.e., those remaining in the quartz grains of the rock when there are no external surface forces on the boundaries of the specimen. The two-dimensional techniques yield secondary principal stresses for the plane of measurement, which here is horizontal and essentially parallel to the bedding. The three-dimensional techniques (Nos. 5 and 6, Table 1) yield the three principal stresses, only one of which,  $\sigma_1$ , it turns out is essentially horizontal.

Before discussing the results, an explanation of the X-ray and photoelastic data is in order. The X-ray analysis of this rock is difficult because the diffraction profiles for {3254} planes are broad and of low intensity. Perhaps this obtains because internal strains exist within the quartz grains as evidenced by profuse development of undulatory extinction and deformation lamellae. Such

## Summary of In Situ and Residual Stress Data - Site No. 1, Rangely Anticline

| Techniques   | Organization                 | $\sigma_1$            | Directions <sup>1</sup> |                       | Magnitudes <sup>2</sup> |            |            | $\sigma_1 - \sigma_3$ |
|--|------------------------------|-----------------------|-------------------------|-----------------------|-------------------------|------------|------------|-----------------------|
|  |                              |                       | $\sigma_2$              | $\sigma_3$            | $\sigma_1$              | $\sigma_2$ | $\sigma_3$ |                       |
| (Bars)   |                              |                       |                         |                       |                         |            |            |                       |
| (Bars)   |                              |                       |                         |                       |                         |            |            |                       |
| <u>Two-Dimensional</u>   |                              |                       |                         |                       |                         |            |            |                       |
| 1. USBM Borehole <sup>3</sup><br>( $\approx 60$ cm) <sup>4</sup> | USGS<br>Menlo Park           | N63°E                 | ...                     | N27°W                 | 5                       | ...        | 3          | 2                     |
| 2. CSIR "Doorstopper"<br>( $\approx 60$ cm)                      | USGS<br>Menlo Park           | N89°E                 | ...                     | N 1°W                 | 17                      | ...        | -14        | 31                    |
| 3. Photoelastic<br>Rosettes<br>(surface)                         | Center for<br>Tectonophysics | N80°E                 | ...                     | N10°W                 | 31                      | ...        | -35        | 66                    |
|  |                              | N75°E                 | ...                     | N15°W                 | 18                      | ...        | 2          | 16                    |
|  |                              | N63°E                 | ...                     | N27°W                 | 30                      | ...        | 21         | 9                     |
|  |                              | N88°E                 | ...                     | N 2°W                 | -8                      | ...        | -18        | 10                    |
|  |                              | N80°E                 | ...                     | N10°W                 | -2                      | ...        | -19        | 17                    |
|  |                              | N84°E                 | ...                     | N 6°W                 | 76                      | ...        | -12        | 19                    |
|  |                              | N69°E                 | ...                     | N21°W                 | 206                     | ...        | -2         | 22                    |
|  |                              | N73°E                 | ...                     | N17°W                 | 177                     | ...        | -8         | 25                    |
|  |                              | N83°E                 | ...                     | N 7°W                 | 217                     | ...        | 5          | 16                    |
| 4. Foil Resistance<br>Rosettes<br>(surface)                      | Center for<br>Tectonophysics | N73°E                 | ...                     | N17°W                 | 25                      | ...        | 11         | 14                    |
|  |                              | N63°E                 | ...                     | N27°W                 | 13                      | ...        | 1          | 12                    |
|  |                              | N88°E                 | ...                     | N 2°W                 | 28                      | ...        | 13         | 15                    |
| <u>Three-Dimensional</u>   |                              |                       |                         |                       |                         |            |            |                       |
| 5. Solid Inclusion<br>(366 cm)                                   | USGS<br>Denver               | Pl. 3°<br>to<br>N41°E | Pl. 24°<br>to<br>N51°W  | Pl. 66<br>to<br>S41°E | 2                       | 1          | -8         | 10                    |
| 6. X-ray Diffraction<br>( $\approx 60$ cm)                       | Center for<br>Tectonophysics | Hor. and<br>N70°E     | Pl. 37°<br>S16°E        | Pl. 54°<br>N26°W      | 2005                    | 30         | -150       | 350                   |

1. Expressed with respect to True North (15° East Declination).

2. For Techniques 1-5 stresses are calculated from strains by use of  $5 \times 10^4$  bars ( $8 \times 10^5$  psi) for Young's Modulus as determined independently by the USGS groups at Menlo Park and Denver, and Poisson's Ratio of 0.15 (Menlo Park) or 0.30 (Denver). Compressive stresses are counted positive.

3. Data represent the average results from six measurements.

4. Depth below surface of outcrop at which measurement was made.

5. Strains detected with X-ray diffractometry are converted to stresses by use of Young's Modulus perpendicular to the {3254} planes in quartz, namely  $9 \times 10^5$  bars. Actual strains are comparable to those measured with foil resistance gages (see text and Figure 2).

6 and 7. Two sets of photoelastic gages were installed within the same 10 cm diameter and were read separately. The values listed first are from the inner and those listed second are from the outer rosettes.

$\bar{\epsilon} = 19 \text{ b}$   
 $s = 15 \text{ b}$

strains are known to produce diffuse diffraction events (Bailey and others, 1958). Because the diffraction profiles are poor, more than the usual number of repeat measurements are needed to determine the mean strains from which the strain quadric is calculated (Friedman, 1967). When the mean value for a given direction is combined with other such mean values, however, they generate through the Eigen-value solution a well defined quadric surface (Figure 2). That is, there are six sets of principal strain axes, each set calculated from a different combination of the normal strain data, and these axes are well grouped on the stereogram (Figure 2). This grouping means that all the measurements are defining a common quadric surface.

The photoelastic gages were read soon after overcoring and several times during the following twenty day interval. The values of the strains varied during this time, but not the orientations of the secondary principal axes. The values listed in Table 1 represent the final readings taken after the rock-gage system had stabilized. At two stations a double set of rosettes were installed within the same 10 cm overcore (see Table 1, footnotes 6 and 7). Soon after overcoring, the inner rosettes show much less strain than the outer ones. The final results for the two stations show the same trend for  $\sigma_1$ . This result enhances the view that the short-time strain relief is dependent upon the proximity of the gages to a free surface.

Examination of Table 1 shows a remarkable degree of agreement in the orientation of  $\sigma_1$  as measured by all six techniques. This stress axis is essentially horizontal and lies within an azimuth range of N 41° E and N 89° E with a mean of N 69° E (calculated from the mean azimuth from each technique). Where reproducibility can be judged, as in the case of the photoelastic and foil-resistance gage measurements, it is excellent relative to the direction of  $\sigma_1$ .

This speaks well not only for these particular measuring systems, but also for the high degree of homogeneity in the direction of the in situ  $\sigma_1$ . Directional relations between the other principal stresses can be compared independently only for the results from the three-dimensional methods. In both cases, the least principal stress  $\sigma_3$  is tensile and inclined at high angles to bedding. However, these axes are  $60^\circ$  apart in the vertical plane oriented nearly normal to the mean  $\sigma_1$  (Table 1).

In contrast to the consistent orientations of the in situ stresses, their magnitudes vary appreciably among and within techniques (Table 1). Excluding the X-ray results, the magnitudes of  $\sigma_1$  range from 31 to -8 bars. On the other hand, the stress difference ( $\sigma_1 - \sigma_3$ ) for the fifteen strain relief measurements ranges from 2 to 66 bars with a mean of 19 bars and a standard deviation of 15 bars. Examination of the data shows that all but two of the fifteen stress-difference values are within one standard deviation of the mean. The variation in stress difference is minimal within the data from the three separate foil-resistance stations. The relatively consistent value for the stress difference coupled with the very consistent orientation of the principal secondary stresses suggests that the variations in magnitudes for the individual stresses reflect the heterogeneity of the in situ state of stress more than the differences among the measuring techniques.

The stress magnitudes calculated for the quartz d-spacing distortions as measured by X-ray diffraction are very large compared to those from the strain-relief data. The large values may arise because of the magnification factor for stresses transmitted across small-area grain contacts (see photoelastic model of residual stress in Ninth Quarterly Technical Report, Figure 4). The actual strains, however,

are of about the same magnitude because the appropriate elastic modulus for quartz is an order of magnitude greater than that for the rock in bulk. For example, the mean stress difference of 19 bars for the fifteen values of  $(\sigma_1 - \sigma_3)$  from the strain-relief data corresponds to a strain of  $330 \times 10^{-6}$ , while the stress difference from X-ray data, 350 bars, gives a strain of  $390 \times 10^{-6}$ . Thus the displacements and resulting strains determined by the two types of measurements are comparable.

To emphasize, the principal stress directions, especially that of  $\sigma_1$ , of the residual strains as measured by X-ray diffraction are similar to those of the in situ state as determined by the strain-relief techniques. This is the first time these measurements have been compared, and the agreement implies that the present-day loads at this outcrop either are negligible or are oriented parallel to the residual stresses. The fact that all the in situ measurements were made within 10 m of a free vertical face enhances the probability that applied loads are very small and that the in situ state of stress is essentially a measure of the residual state. Because the X-rays sense strains locked in the quartz grains by secondary cementation or grain contact welding, it is reasonable to conclude that the residual strains date from the time the grains were cemented under load (Friedman, in press).

The N 70° E bearing of  $\sigma_1$  for both the in situ and residual states of stress at Site No. 1 does not agree with the  $\sigma_1$  direction inferred from focal plane solutions of man-induced earthquakes in the Rangely Field (Raleigh and others, 1970, p. 660-661). The earthquakes occur as a result of the waterflooding which has raised the reservoir fluid pressure to 0.6 of the overburden pressure in the Weber sandstone (Pennsylvanian). In September 1969, a network of 14 stations was

installed by the U. S. Geological Survey, National Center for Earthquake Research. Using the data from this network, Raleigh and his associates have established that the principal seismic activity occurs "over a depth interval of 1 to 4 km along a vertical fault which cuts across the field. The earthquake epicenters are located on the southern margin of the field and die out toward the interior... Focal-plane solutions indicate right-lateral, strike-slip faulting." Thus the inferred  $\sigma_1$  for this faulting would tend to parallel the anticlinal axis, N 45° W to N 60° W (C. B. Raleigh, personal communication, 1970), as opposed to the N 70° E trend at Site No. 1. It should be noted, however, that this site is located at the surface at the opposite end of the field.

The average trend of the in situ  $\sigma_1$ , N 70° E, is subparallel to macrofractures making up the E-W group (Figure 1). At the level of the individual measurement, however, the in situ  $\sigma_1$  does not parallel any of the nearest macrofractures. This result is particularly well documented in the case of the photoelastic-gage measurements because previous work with similar gages had suggested the parallelism and Dr. Brown was aware of that result (John Handin, personal communication, 1970).

On the other hand, the N 70° E trend is but 25° from normal to the fold axis which trends N 45° W at Site No. 1. Indeed,  $\sigma_1$ , from the solid inclusion gage (Table 1, Technique No. 5) is perpendicular to the fold axis. Dynamic petrofabric analyses around the noses of plunging anticlines (e.g., Carter and Friedman, 1965) typically show that derived compression axes ( $\sigma_1$  axes) tend to lie parallel to bedding and to be skewed to the major fold axes in the same sense that the N 70° E direction deviates from the perpendicular to the fold axis (N 45° E). Moreover, the N 70° E direction is the acute bisector between two of the three

fracture sets present in the outcrop (N 44° E and E-W, Figure 1). Hence it is reasonable to conclude that the in situ  $\sigma_1$  is residual and reflects the stresses in the beds at the time of folding. This also implies that the quartz grains were cemented by pressure solution of grain contacts during folding.

### Fracture Anisotropy in the Mesa Verde Sandstone

In light of the extensive data on in situ and residual strains in the Mesa Verde sandstone we have tested several samples to determine if the rock is anisotropic relative to induced fractures, and if so, whether the trend of induced fractures can be predicted from the superposition of the applied load on the prestress (Friedman and Logan, 1969). Toward this end 18 oriented discs, each 2.54 cm in diameter and about 2.0 cm long, were prepared from cylinders cored perpendicular to bedding. Each disc was loaded at its center by opposed ball bearings until it fractured. Some discs failed along a simple fracture, others along two fractures and still others by three radiating fractures. In total, 44 fractures occurred in the 18 discs. The trace of each fracture on the circular section of the disc (i.e., the bedding plane) was recorded and plotted on a circular frequency diagram. The resulting plot shows a strong tendency for the rock to fracture at N 30° W to N 50° W (Figure 3).

The N 70° E trend for the induced fractures should obtain if they form with respect to the superposition of the applied load on the prestress. That is, tensile fractures should parallel the plane containing the net  $\sigma_1$ , and intermediate stress,  $\sigma_2$ . The applied point-load produces a net  $\sigma_1$  that is normal to the circular section of each disc and an axially symmetric tensile stress parallel to the circular section. These tensile stresses are superposed on the prestresses.

Since the greatest compression of the prestress trends N 70° E the net  $\sigma_2$  at the time of fracture will also be parallel to this direction. Since the fractures do not form along this direction, they cannot be related to the prestress.

An anisotropy in grain elongation can control the induced fractures (Friedman and Logan, 1970). Accordingly, azimuths were recorded for the apparent long axes in grains with dimensional axial ratios of  $\geq 2:1$  in thin sections cut parallel to the circular section of the discs, i.e., parallel to the bedding. Resulting circular frequency diagrams (Figures 3b and 3c) indicate that the induced fractures also are ignoring the grain-shape fabric in the rock. This dimensional anisotropy within the bedding plane may produce an anisotropy in elastic constants. Such an anisotropy has not been considered in the analysis of the strain-relief data.

The induced fractures (N 30° W - N 50° W) do correlate geometrically, however, with one of the major fracture sets at Site No. 1, namely those striking N 26° W, and they are subparallel to the fold axis (N 45° W).

### Residual Strain and Fracture Propagation

Previous work on Task I has demonstrated that the residual elastic strains locked in the quartz grains of sandstones can under certain conditions of external loading influence the orientations of experimentally induced fractures (Friedman and Logan, 1970). This result implies that the residual strains are a source of energy for fracture that should be considered along with the strain energy from applied loads and the energy to create new surface. The design of an experimental program to evaluate the role of residual strains in tensile fracture is outlined in our Sixth Quarterly Technical Report (May, 1969, p. 2-5). In our Ninth Quarterly Technical Report (February, 1970, p. 2-9) we reported on the first phase of this study, namely, that the residual strains did in fact relax all or in part within a distance of 4.5 mm on either side of an induced tensile fracture. In these tests the fractures were induced crudely by bending notched beams without any control of the energy input. This was an important step, however, because it was necessary to demonstrate that the residual strains were indeed released upon passage of a fracture, and hence that they probably did contribute energy to fracture initiation and propagation. On the basis of these tests we designed and constructed an apparatus to obtain stable tensile fracture such that the external energy to fracture the rock could be measured accurately from the force versus displacement curve. Energy losses in the form of heat and sound are small and are neglected. Knowing the energy input, one can then quantitatively compare it with the change in residual strain adjacent to the fracture as determined by X-ray measurements before and after fracturing. In addition, by carefully determining the area

of the fracture surface one can determine the surface energy of the rock and compare it to lithology, texture and fabric.

To achieve stable fracturing one must be able to propagate the fracture at will, and this requires a testing machine of very high stiffness. One can effectively stiffen the machine in several ways. The simplest and cheapest method suitable to our application is parallel loading of a thick steel beam and the notched rock beam (Figure 4).

In our device the force is applied by a 100 ton hydraulic press through the thrust block to the four-point loaded steel beam, the dimensions of which are so chosen that the force required to deflect it is about 50 times larger than the force needed to deflect the rock beam the like amount. The force on the three-point loaded, notched rock beam is measured by the gauge located between the beams. The mid-point deflection is determined by a transducer that measures the relative displacement between the force-gauge rod and one of the rods supporting the rock test-beam. For our purpose the error of this measurement relative to the true deflection of the top surface of the beam is negligible, and the accuracies of both force and deflection measurements are better than 1 percent.

The first series of tests was designed to determine if stable fractures could indeed be made, and if so, to evaluate reproducibility and the effect of the notch depth, and to compare our values for the fracture-surface energy with others previously published. This work is currently underway. As the complete force-deflection curve shows (Figure 5), we have created stable fracture in prisms of Tennessee sandstone, and our value for the fracture-

surface-energy is in excellent agreement with data determined by a quite different experimental loading scheme (Perkins and Krech, 1966). The energy considerations involved in tensile fracture propagation in a notched bar and the distinctions between catastrophic, semistable, and stable fractures are given by Nakayama (1965) and by Moavenzadeh and others (1966), and need not be repeated here.

The initial test made after calibration was on a prism of Tennessee sandstone (10.2 x 2.54 x 1.40 cm) containing a notch 3.6 mm deep and 0.9 mm wide. This specimen was bent at the slowest rate of piston displacement ( $4 \times 10^{-4}$  cm/sec). The force-deflection curve shows the shape typical of stable fracture (Figure 5). Careful examination of the specimen reveals that only one fracture has formed from the notch tip and no "side cracking" or additional fracturing that have complicated previous observations (Moavenzadeh and others, 1966). The area under this curve  $U$  represents the external energy needed to fracture the rock. On the assumption that sonic and thermal energy losses are negligible,  $U$  is related to the effective fracture surface energy  $\gamma_{eff}$  as follows:

$$U = 2A\gamma_{eff}, \quad (1)$$

where  $A$  is the area of one of the fracture surfaces. Thus, if the area of the fracture surface is known,  $\gamma_{eff}$  can be calculated.

A simple calculation of the nominal fracture area (2.54 cm x [1.4 - 0.36] cm = 2.64 cm<sup>2</sup>) gives too small a value because the fracture surface is irregular. That is, the fracture has propagated around as well as through

the quartz grains. In order to obtain a more accurate estimate of the true area, lengths along the irregular surface as viewed on edge were measured optically at 100X magnification with the aid of a calibrated eyepiece micrometer. Repeated measurements at several cross sections indicate that the actual length along the surface is 1.34 times the straight-line length. Thus, the corrected area is  $4.73 \text{ cm}^2$ . Using this area in Eq. (1) and the value of  $U$  measured from the curve (Figure 5) with a polar planimeter, we obtain for  $\gamma_{\text{eff}}$  the value of  $3.8 \times 10^4 \text{ ergs/cm}^2$ .

Perkins and Krech (1966) had already determined  $\gamma_{\text{eff}}$  for Tennessee sandstone and a few other sedimentary rocks using the Gilman (1960) cleavage technique. This is the same experimental method used by Brace and Walsh (1962) and by Santhanam and Gupta (1968) in their studies of surface energies in quartz and calcite, respectively. In this test a rectangular specimen with a deep saw cut is pulled perpendicular to the plane of the cut. The beams act as cantilevers, and the tensile fracture propagates from the tip of the saw cut as the tension is increased. For the Tennessee sandstone at zero confining pressure Perkins and Krech determined  $\gamma_{\text{eff}}$  to  $8.8 \times 10^4 \text{ ergs/cm}^2$ . They apparently used the nominal area of the newly created fracture surface in their calculation, and hence their value is probably too large. Had we also used the nominal area, we would have obtained a value of  $7.1 \times 10^4 \text{ ergs/cm}^2$ , in good agreement.

The surface energy for fracture in sandstone is one to two orders of magnitude greater than the surface energies associated with cleavages in quartz single crystals (Brace and Walsh, 1962). Why then should fractures propagate along grain boundaries as well as through grains? Perkins and

Krech (1966, p. 311) have suggested that the larger amount of energy is "absorbed by various inelastic and dissipative processes occurring near the extending edge of the crack," and they prefer to speak of "apparent surface energy." This question can be resolved only by further work.

During the next Quarter we plan to (a) test for reproducibility of  $U$  and  $\gamma_{eff}$  values, (b) evaluate the effect of the notch depth on values of  $\gamma_{eff}$ , (c) determine if we can create stable fractures in other rocks, and (d) begin to correlate measurements of  $U$  with the change in residual elastic strain energy.

#### States of Stress in Granular Aggregates

Deeper understanding of the relations between stress patterns in two-dimensional photoelastic aggregates and those in natural aggregates has resulted from study of microfractures in experimentally deformed, spherical glass beads. The study demonstrates that the distributions of maximum stress difference and of microfractures in spherical glass grains are independent of both the scale and material. Both of these distributions are most strongly influenced by the nature of contacts with neighboring grains. Number, position, and other characteristics of contacts, but especially the load conditions at contacts relate to the manner in which boundary loads are transmitted through the aggregate. These observations combined with the extension-fracture criterion developed earlier (Sixth Quarterly Technical Report) permit definition of stress states and prediction of corresponding microfracture patterns in grains as functions of packing and loading.

Microfracture patterns in experimentally deformed glass beads have strong resemblance to those predicted by the photoelastic study. This strong resemblance implies that the extension-fracture criterion can be tended to include three-dimensional aggregates. Furthermore, the criterion holds for a wide range of experimental conditions including confining pressures to 1000 bars, strain to 17.7 percent, and various combinations of grain sizes (Table 2). It is possible, therefore, to use microfracture arrays within deformed grains to derive the dominant packing arrangement (cubic or hexagonal) at the time of fracturing as well as the directions and relative magnitudes of loads applied to the aggregate.

Fracture patterns in the glass spheres resemble extension fracture configurations predicted from photoelastic study. Photoelastic displays in typical inner discs of cubic arrays (Figure 6) and expected fracture patterns for various load conditions (Figure 7) are distinct from those for hexagonal arrays (Figure 8) except for  $P_1$  very much less than  $P_2$ , in which case horizontal fractures ought to form in grains of both arrays. These considerations suggest that fracture patterns in grains must reflect packing arrangement as well as the orientations and relative magnitudes of loads applied at the boundaries of the aggregate. The latter relations to boundary loads were established in the Ninth and Tenth Quarterly Reports.

Experimentally deformed specimens provide a test for application of these ideas to three-dimensional, small-scale, and more natural examples. Neighboring beads which contribute to microfracture of a sphere are often seen in thin section (Figure 9). Here the relation of fractures to critical contacts is visually verified, and fracture patterns are seen faithfully to

reflect configurations predicted from photoelasticity. For example, the major fracture in Figure 9 is like that predicted in Figure 7c. More often, at least one neighboring grain which has contributed to microfracture is not visible in the plane of section (Figures 10 and 11). Even here it is possible to use fracture patterns in a grain to determine the minimum number of critical contacts acting on the grain.

Some beads are complexly fractured. Most of these appear to contain two or more superposed predicted fracture patterns. Contacts not in the plane of section typically influence such complex patterns (Figure 11). The remainder of complexly deformed spheres are so highly fractured that comparison with predicted patterns is impossible (Figure 12). However, most of these crushed beads are not fractured in their central regions, which is predictable from photoelastic data for discs with many critical contacts. Compare the unfractured center of the bead in Figure 11 with the isotropic areas in the centers of discs in Figure 8a, b, and c and the respective fracture predictions. Even in crushed spheres, some trends are still recognizable as dominant.

Using fracture patterns as guides, one may infer the packing of neighbors around a grain. For example, the pattern in Figure 11 suggests hexagonal packing, and the pattern in Figure 13 implies cubic packing. The realization that fracture orientations within grains of an aggregate depend upon packing permits better interpretation of fracture patterns within individual grains. This realization also leads to better understanding of variations of fracture patterns within individual grains as well as variations of fracture orientations for the aggregate as a whole. These concepts will be applied to aggregates of spherical beads and sand aggregates in Technical Report Number 3 (in preparation).

TABLE 2  
Experimentally Deformed Glass Spheres

| Experiment<br>Number | Average<br>Grain<br>Size<br>(mm) | Confining<br>Pressure<br>(bars) | Strain<br>at<br>Termination<br>(percent) | Specimen<br>Length<br>(cm) |
|----------------------|----------------------------------|---------------------------------|--|----------------------------|
| 1                    | 0.6 <sup>1</sup>                 | 172                             | 3.1                                      | 2.54                       |
| 2                    | 0.6                              | 172                             | 3.2                                      | 2.54                       |
| 3                    | 0.6                              | 345                             | 3.0                                      | 2.67                       |
| 4                    | 0.3 <sup>2</sup>                 | 345                             | 2.8                                      | 2.84                       |
| 5                    | 0.6                              | 345                             | 6.0                                      | 2.54                       |
| 6                    | 0.3                              | 345                             | 6.3                                      | 2.56                       |
| 7                    | Mixed <sup>3</sup>               | 345                             | 6.4                                      | 2.44                       |
| 9                    | 0.6                              | 345                             | 0.0                                      | 2.54                       |
| 15                   | 0.6                              | 1,000                           | 12.8                                     | 2.54                       |
| 17                   | 0.6                              | 1,000                           | 17.7                                     | 2.03                       |
| 18                   | 0.6                              | 1,000                           | 13.9                                     | 2.03                       |
| 19                   | 0.6                              | 1,000                           | 12.6                                     | 2.03                       |
| 20                   | 0.6                              | 1,000                           | 15.2                                     | 2.03                       |
| 21                   | 0.3                              | 1,000                           | 7.3                                      | 2.03                       |
| 24                   | Mixed                            | 1,000                           | 0.0                                      | 2.03                       |
| 26                   | 0.6                              | 1,000                           | 0.0                                      | 2.57                       |
| 27                   | 0.6                              | 1,000                           | 0.0                                      | 2.57                       |
| 28                   | 0.6                              | 1,000                           | 0.0                                      | 2.57                       |
| 29                   | 0.6                              | 1,000                           | 6.0                                      | 2.60                       |

All experiments were done in compression at room temperature and a strain rate of  $10^{-4}$ /sec. All specimens were encased in cylindrical copper jackets and were about 1.27 cm in diameter.

1. The size of large glass spheres ranges from 0.5 to 0.7 mm.
2. The size of small glass spheres ranges from 0.25 to 0.35 mm.
3. Mixed specimens consist of 50 weight percent each of large and small spheres.

Packing arrangement also plays a role in the alignment of microfractures. Photoelastic arrays suggest that microfractures in adjacent grains ought to connect at critical contacts (for example, see Figure 1 on page 7 of the Eighth Quarterly Technical Report). This tendency has been noted in experimentally deformed glass beads (Figure 14). The significance of these connected fractures will be examined more closely where the orientations of fracture chains relative to the greatest load axis will be compared with other microfracture data.

### TASK III

#### Summary

Triaxial compression tests have been done on Westerly granite and Solenhofen limestone at intermediate strain rates from  $10^{-2}$  to 1/sec and at confining pressures to 7 and 3 kb, respectively. From these preliminary data, both rocks show 1) an increase of ultimate strength with increasing confining pressure, as had been demonstrated long ago in static tests; 2) an increase of ultimate strength with increasing strain rate at all confining pressures; and 3) a greater rate of increase of strength with increasing strain rate at the higher confining pressures. Westerly granite shows an increase of the elastic modulus with increasing strain rate when the specimen is unconfined, but the Solenhofen limestone does not. Westerly granite is brittle under all test conditions. Solenhofen limestone becomes ductile at about 1 kb at a strain rate of  $10^{-4}$ /sec, and this transition appears to increase to about 1.5 kb at a strain rate of 1/sec.

### Tests on Westerly granite

The block of granite used here is identical to that used by Friedman, Perkins, and Green (1968) and already described by them. Figure 15 shows typical piston force and displacement versus time records for the granite which is brittle under all the test conditions imposed. Axial strain rates are calculated from average displacement rates determined by the proximator and corrected for apparatus distortion. Axial differential stresses are calculated from forces measured by the external gage and corrected for changes in the cross-sectional areas of the deforming specimens. Fracturing of the specimen is accompanied by a loss of cohesion and a rapid rise in the displacement rate until the loading piston is stopped.

Derived stress-strain curves at average strain rates of  $10^{-2}$ ,  $10^{-1}$ , and 1/sec are shown in Figures 16, 17, 18, respectively. For a given strain rate, the ultimate strength increases with increasing confining pressure. This behavior is consistent with that observed previously at static strain rates of  $10^{-4}$  and  $10^{-7}$ /sec (Brace and Martin, 1968; Byerlee, 1966; Mogi, 1967; Brown and Swanson, 1970). At a constant confining pressure, the ultimate strength increases as the strain rate is increased from  $10^{-2}$  to 1/sec. This same behavior was reported (Brace and Martin, 1968) at strain rates of  $10^{-7}$  and  $10^{-4}$ /sec. The elastic modulus, as determined from the stress-strain curves, increases as the strain rate increases when the specimen is unconfined. This behavior has also been observed previously (Green and Perkins, 1969) under the same conditions. As the confining pressure is increased, this effect is suppressed until at 3 kb, it is indiscernible.

If rock-properties research is to be accomplished efficiently, then clearly the data of different workers in different laboratories must be validly comparable, especially when experimental conditions do not overlap. This requires that all tests be done on the same material. As an example, consider Figure 19 where ultimate strength is plotted against confining pressure at strain rates of  $10^{-2}$ ,  $10^{-1}$ , and 1/sec along with Brown and Swanson's data (1970) from two other blocks of Westerly granite tested at  $10^{-4}$ /sec. Notice that the maximum increase in strength associated with the 100-fold increase in strain rate from  $10^{-2}$  to 1/sec is about 20 percent, only a little greater than the variation in strength between the two different blocks tested at the same strain rate, namely  $10^{-4}$ /sec. Clearly our results are not comparable with those of Brown and Swanson, and we would have to repeat their perfectly good experiments on our block of granite to obtain relevant data at  $10^{-4}$ /sec. This discrepancy need not be and almost surely is not due to differences in experimental techniques. It is due to variations in the fabrics (mineral composition, grain size, degree of preferred orientations of minerals, etc.) of the several blocks of rock which were collected without regard for inter-laboratory correlations.

Note that the rate of increase of strength with confining pressure rises with strain rate from  $10^{-2}$  to 1/sec. A similar effect in sandstone has recently been observed by Swanson (personal communication, October 1970).

Although again because of the lack of a standard test material comparisons must be made cautiously, we have plotted the square root of the second deviatoric stress invariant against mean pressure at fracture

as derived from shock, intermediate strain-rate, and static tests (Figure 20). The spread of the data considered, about all one can conclude is that the slopes of the curves are generally consistent.

#### Tests on Solenhofen limestone

To date a few tests have been done on Solenhofen limestone at confining pressures to 3 kb and strain rates from  $10^{-2}$  to 10/sec on a block furnished by E. C. Robertson. Depending upon the composition, fabric, and strain rate, this rock has a brittle-ductile transition between 0.75 and 2 kb at room temperature. The force and displacement records for brittle behavior have the same characteristics as those of Westerly granite. Within the ductile regime, the force-displacement history of the specimen changes as the rock passes through the yield stress (Figure 21). The displacement rate increases by a factor of two to eight. Ductile flow is terminated when the loading piston is stopped. The strain rate in the inelastic region has been used in plotting the present data. Conjugate sets of shear fractures are characteristic of the brittle and transitional behavior (Figure 22). Through-going fractures develop along one of these shear zones as shortening progresses. Ductile deformation is accomplished by intracrystalline flow.

Characteristic stress-strain curves at a strain rate of  $10^{-1}$ /sec are shown in Figure 23. Although only preliminary data have been analyzed, it appears limestone and granite behave differently in the elastic region. No evidence of a change in elastic modulus is found with increasing strain rate. The ultimate strength increases with both strain rate and confining pressure as previously observed at static strain rates of  $10^{-7}$ /sec to  $10^{-4}$ /sec (Green and Perkins, 1969). The rate of increase of strength with increasing strain rate rises as the confining pressure increases.

Heard (1960) shows that this rock undergoes the brittle-ductile transition at about 1 kb confining pressure. Handin, Heard, and Magouirk (1967) show that this transition is lowered to about 0.75 kb as the strain rate is lowered three orders of magnitude. Although the problem of lithologic variation again arises when one attempts to compare data from several sources, our preliminary stress-strain data suggest that the transition pressure is raised to 1.5 to 2 kb when the strain rate is increased to 1/sec.

#### Future work

During the next quarter we plan to 1) extend the tests on granite and limestone to the highest achievable strain rates, and 2) to begin assembling the pore-pressure equipment.

## REFERENCES

- Bailey, S. W., Bell, R. A., and Peng, C. J., 1958, Plastic deformation of quartz in nature: Geol. Soc. America Bull., v. 69, p. 1443-1466.
- Brace, W. F., and Martin, R. J. III, 1968, A test of the law of effective stress for crystalline rocks of low porosity: Int. Jour. Rock Mechanics, v. 5, p. 415-426.
- Brace, W. F., and Walsh, J. B., 1962, Some direct measurements of the surface energy of quartz and orthoclase: Am. Mineralogist, v. 47, p. 1111-1122.
- Brown, W. S., and Swanson, S. R., 1970, Constitutive equations for Westerly granite and Cedar City tonalite for a variety of loading conditions: DASA Report 2473, 118 p.
- Byerlee, J. D., 1966, Frictional characteristics of Westerly granite: Ph.D. Dissertation, Massachusetts Institute of Technology, Cambridge.
- Carter, N. L., and Friedman, M., 1965, Dynamic analysis of deformed quartz and calcite from the Dry Creek Ridge Anticline, Montana: Am. Jour. Sci., v. 263, p. 747-785.
- Friedman, M., 1967, Measurement of the state of residual elastic strain in rocks by X-ray diffractometry: Norelco Reporter, v. 14, p. 7-9.
- Friedman, M., in press, X-ray analysis of residual elastic strains in quartzose rocks: Proc. Tenth Symposium on Rock Mechanics, Austin, Texas, May 1968.
- Friedman, M., and Logan, J. M., 1970, Influence of residual elastic strain on the orientation of experimental fractures in three quartzose sandstones: Jour. Geophys. Res., v. 75, p. 387-405.
- Friedman, M., Perkins, R. D., and Green, S. J., 1968, Observations of brittle-ductile deformation features at the maximum stress of Westerly granite and Solenhofen limestone: MSL-68-43, Materials and Structures Laboratory, General Motors Corporation.
- Gilman, J. J., 1960, Direct measurement of the surface energies of crystals: Jour. Appl. Phys., v. 31, p. 2208-2218.
- Green, S. J., and Perkins, R. D., 1969, Uniaxial compression tests at strain rates from  $10^{-4}$ /sec to  $10^4$ /sec on three geologic materials: DASA-2199, Materials and Structures Laboratory, General Motors Corp., MSL-68-6.

- Green, S. J., and Perkins, R. D., in press, Uniaxial compression tests at strain rates from  $10^{-4}$  to  $10^4$ /sec on three geologic materials: Proc. Tenth Symposium on Rock Mechanics, Austin, Texas; May 1968.
- Gregson, V. G. Jr., Green, S. J., Isbell, W. M., 1969, Effect of material strength on wave propagation in rocks: Progress Report No. 19, Contract DA-49-146-XZ-544, Materials and Structures Laboratory, General Motors Corp.
- Handin, J., Heard, H. C., and Magouirk, J. N., 1967, Effects of the intermediate principal stress on the failure of limestone, dolomite and glass at different temperatures and strain rates: Jour. Geophys. Res., v. 72, p. 611-640.
- Heard, H. C., 1960, Transition from brittle to ductile flow in Solenhofen limestone as a function of temperature, confining pressure and interstitial fluid pressure: Geol. Soc. Am. Mem. 79, p. 193-226.
- Leeman, E. R., 1970, Experience through the world with the CSIR "door-stopper" rock stress measuring equipment: Proc. 2nd International Congress on Rock Mechanics, v. 2, paper 4-6.
- Merrill, R. H., 1967, Three-component borehole deformation gage for determining the stress in rock: U. S. Bur. Mines, RI 7015, 38 p.
- Moavenzadeh, F., Williamson, R. B., and Wissa, A. E. Z., 1966, Massachusetts Inst. Tech., Research Report R66-56, 85 p.
- Mogi, K., 1967, Effect of the intermediate principal stress on rock failure: Jour. Geophys. Res., v. 72, p. 5117-5131.
- Nakayama, Junn, 1965, Direct measurement of fracture energies of brittle heterogeneous materials: Jour. Am. Ceramic Soc., v. 48, p. 583-587.
- Nichols, T. C. Jr., Abel, J. F. Jr., and Lee, F. T., 1968, A solid inclusion borehole probe to determine three-dimensional stress changes at a point in a rock mass: U. S. Geol. Surv. Bull. 1258-C, p. C1-C28.
- Obert, Leonard, 1966, Determination of stress in rock - A state-of-the-art report: Am. Soc. Testing Materials, STP 429, 56 p.
- Perkins, T. K., and Krech, W. W., 1966, Effect of cleavage rate and stress level on apparent surface energies of rocks: Soc. Pet. Eng. Jour., v. 237, p. 308-314.
- Raleigh, C. B., Bredehoeft, J., Healy, J. H., and Bohn, Joyce, 1970, Earthquakes and waterflooding in the Rangely Oil Field: Geol. Soc. America, Abstracts with Programs, v. 2, no. 7, p. 660-661.

Santhanam, A. T., and Gupta, Y. P., 1968, Cleavage surface energy of calcite:  
Int. Jour. Rock Mechanics, v. 5, p. 253-259.

Voight, Barry, 1967, On photoelastic techniques, in situ stress and strain  
measurement, and the field geologist: Jour. Geol., v. 75, p. 46-58.

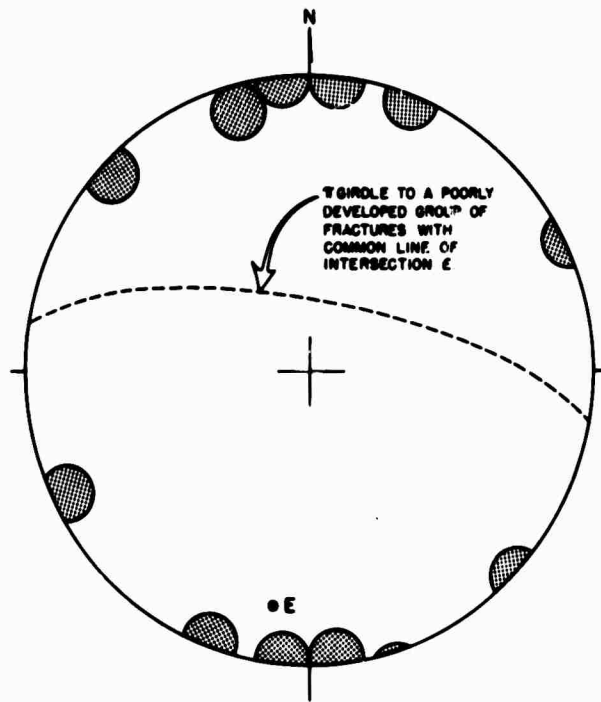


Figure 1 - Stereogram shows average orientation of macrofracture sets at Site No. 1, Rangely Anticline. Plane of the diagram is horizontal with data plotted in lower hemisphere, equal-area projection. Each stippled circle represents the center of a concentration of normals to macrofractures. Total number of individual fracture measurements is 100.

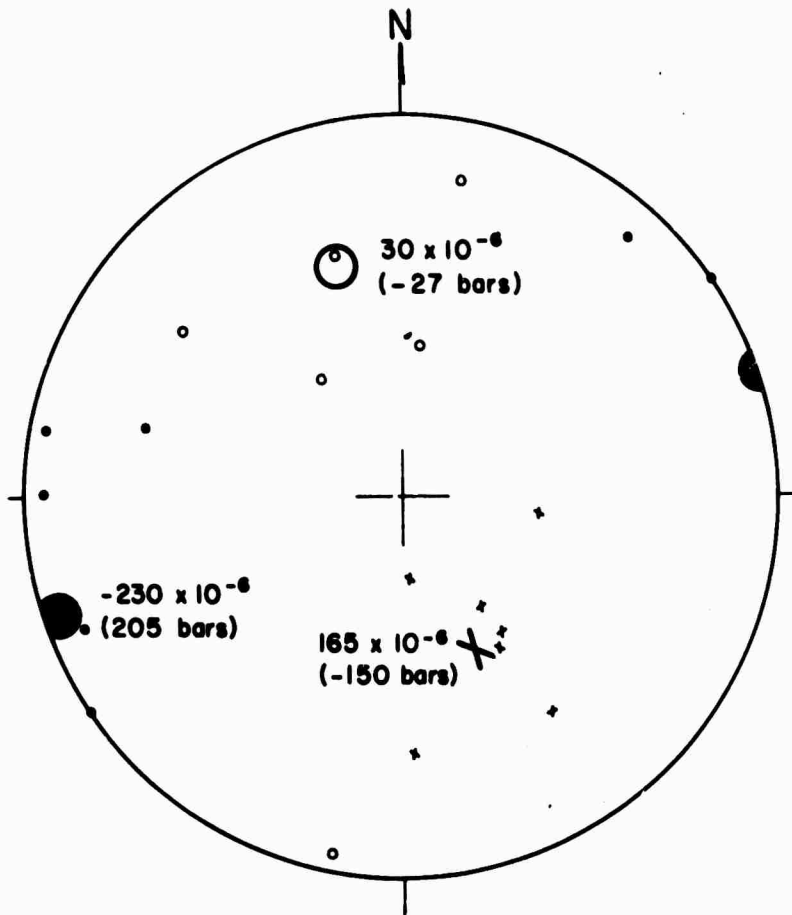


Figure 2 - Stereogram shows orientation of individual and average principal strain axes that define the residual state of elastic strain in the Mesa Verde sandstone, Site No. 1, X-ray diffraction technique. Plane of the diagram is horizontal; data are plotted in upper hemisphere equal-area projection. Symbols x, o, and • indicate the greatest, intermediate and least principal elongations, respectively. The large X, O and • mark the mean orientations and magnitudes calculated from the six sets of individual principal axes. Note the individual axes are reasonably grouped about each mean position.

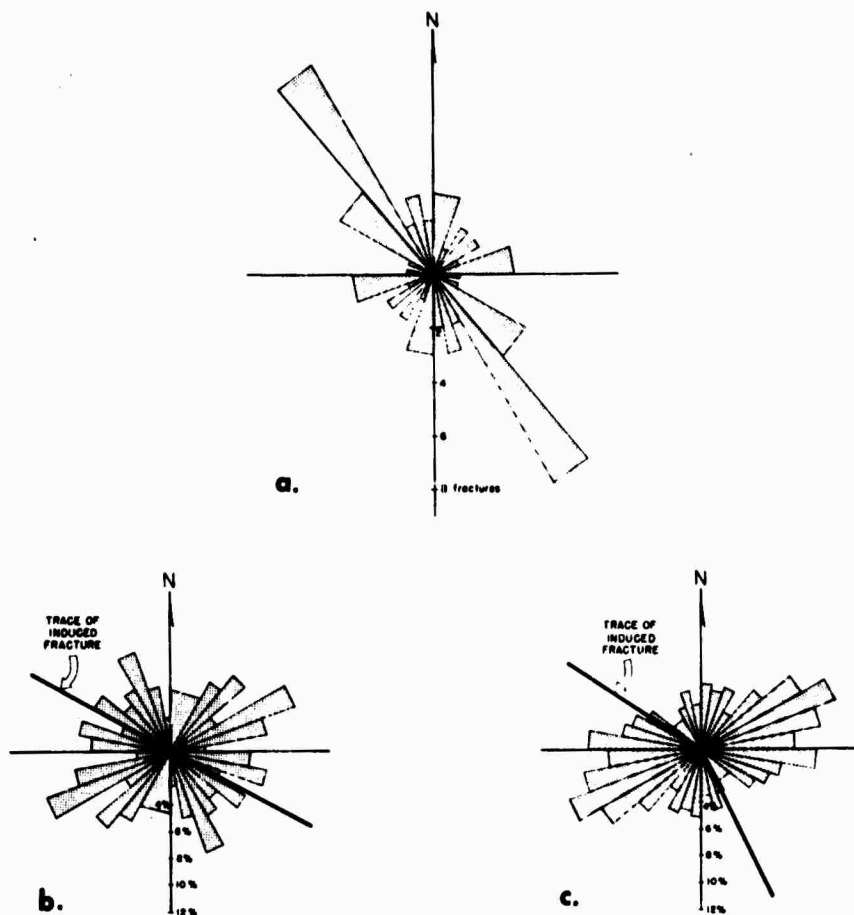


Figure 3 - Circular histograms show the frequency distribution of the azimuths to 44 induced fractures in circular discs, point-load tests in (a) and the trends of apparent long axes of 200 grains with dimensional long to short axis ratios of  $\geq 2:1$  in each (b and c). Plane of each diagram is horizontal, i.e., parallel to the bedding plane of the Mesa Verde sandstone.

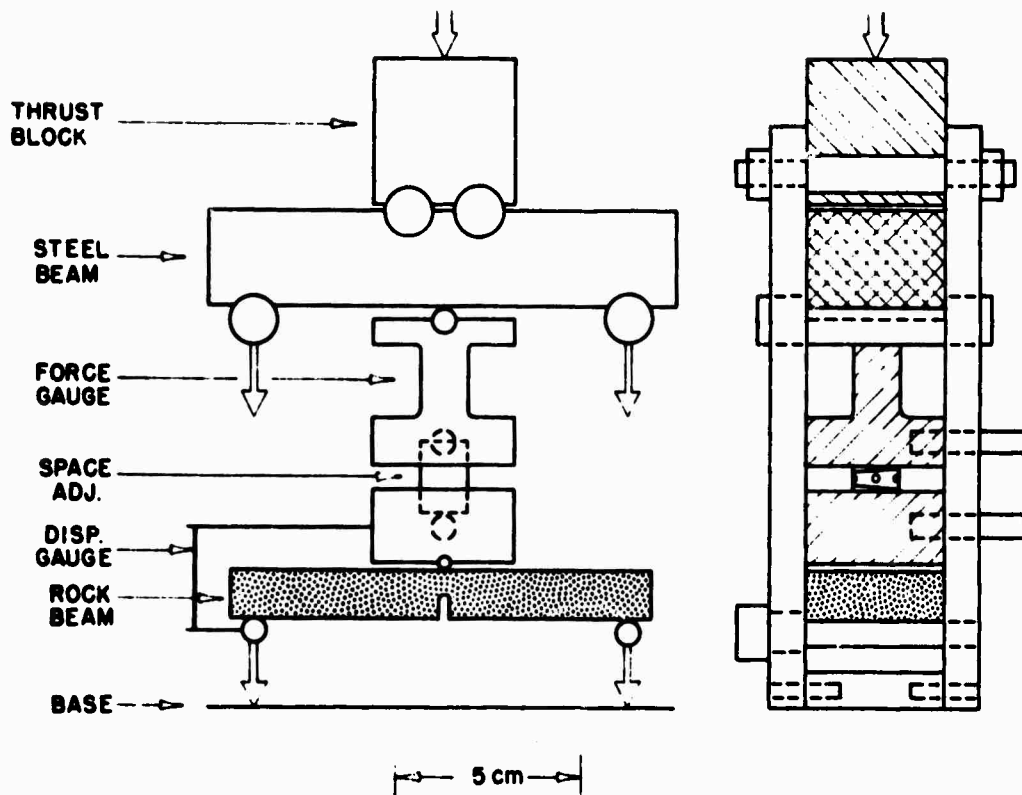


Figure 4 - Schematic diagram of the parallel beam loading device.

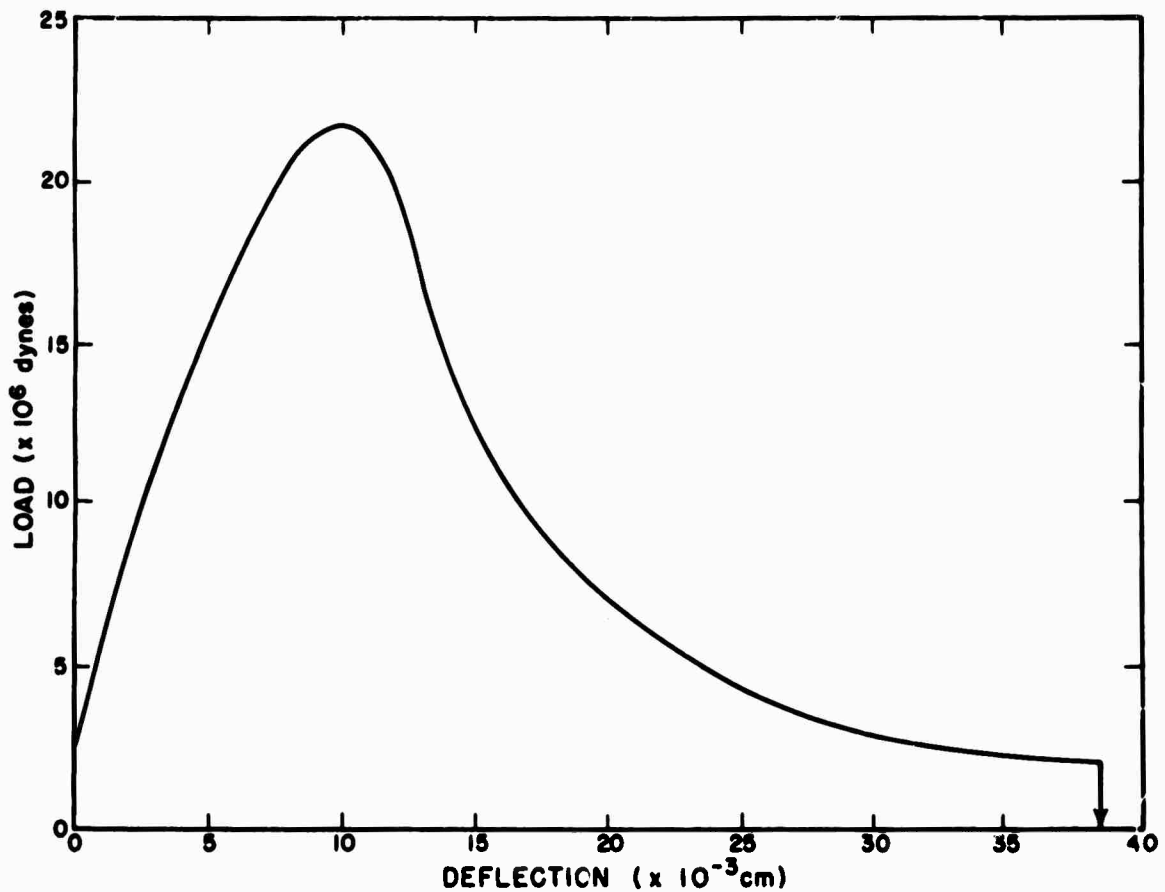


Figure 5 - Bending load versus deflection for tensile fracture of Tennessee sandstone. Shape of curve is typical of stable fracture. Area under curve is external energy required to fracture the rock. The zero-deflection intercept represents the weight of the force gauge.

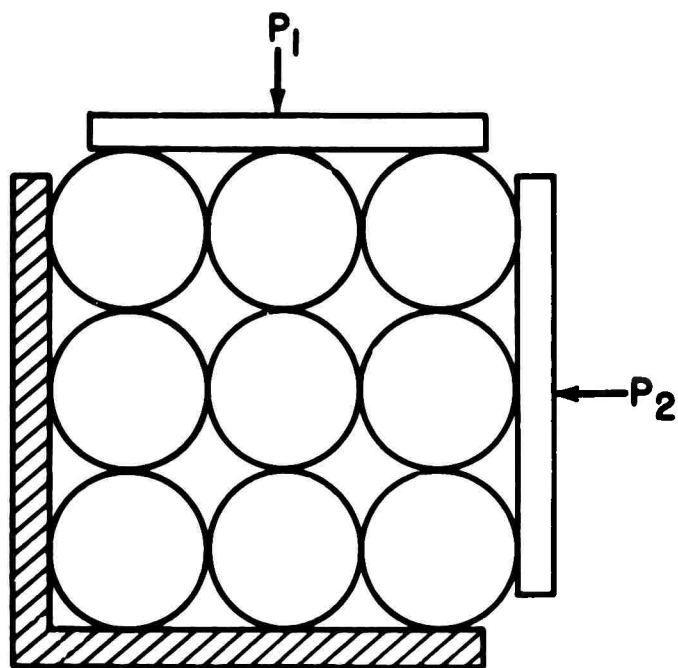


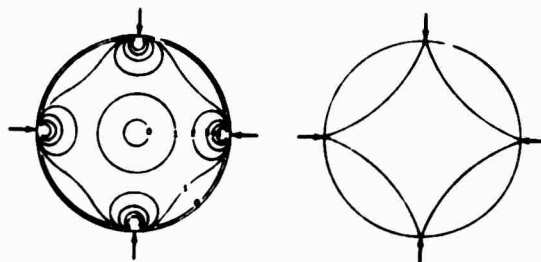
Figure 6. Cubic packing of circular discs. If  $P_1$  and  $P_2$  are nearly the same magnitude, all discs are in contact with all their neighbors. If  $P_1$  is sufficiently greater than  $P_2$  then very little load is exerted at horizontal contacts and discs may not touch horizontally. This latter situation is defined as  $P_1 \gg P_2$ .

Loading  
Condition

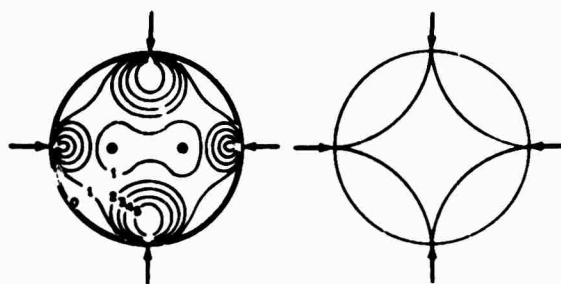
Photoelastic  
Fringe  
Pattern

Expected  
Fracture  
Pattern

(a)  
 $P_1 = P_2$



(b)  
 $P_1 > P_2$



(c)  
 $P_1 \gg P_2$

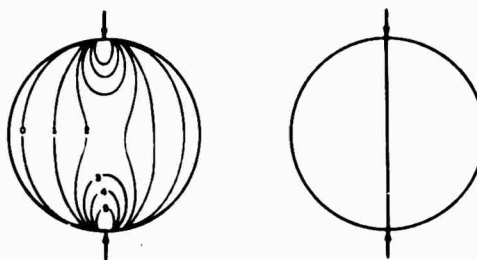


Figure 7. Fringes and expected fractures for typical inner discs in cubic arrays. ( $P_1$ ,  $P_2$  and the meaning of  $P_1 \gg P_2$  are defined in Figure 6.)

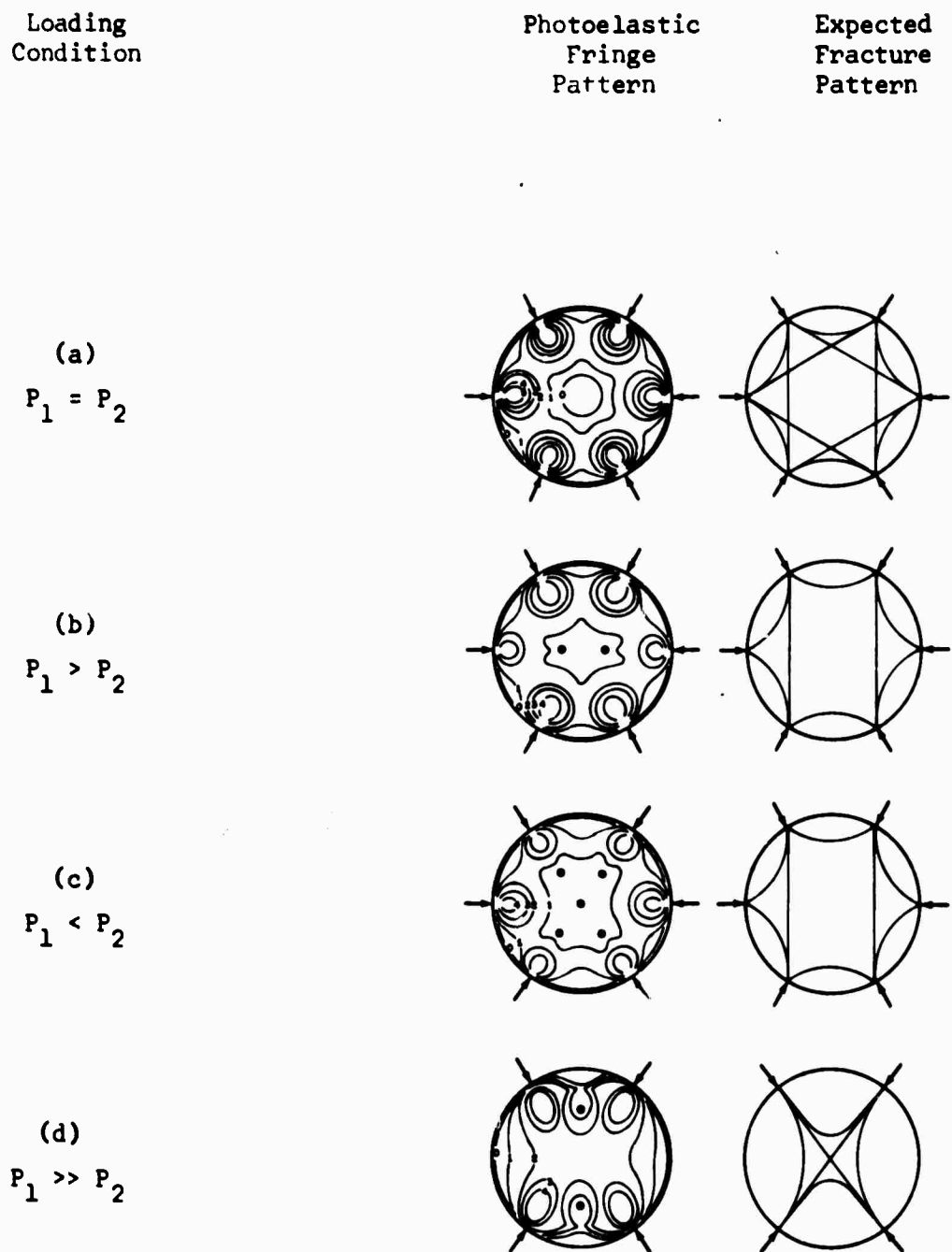


Figure 8. Fringes and expected fractures in typical inner discs of hexagonal arrays. ( $P_1$  and  $P_2$  are defined in Figure 6.) All six contacts with neighbors are significant influences on fringe patterns for (a), (b), and (c). The horizontal contacts are not significant influences on fringes for (d).



NOT REPRODUCIBLE

**Figure 9.** Microfracture resulting from diametral load. The major fracture in the central sphere probably resulted from one pair of critical contacts. The grains adjacent to the central sphere appear to be arranged in cubic packing. The central sphere is 0.3 mm in diameter. This specimen (Experiment number 6 on Table 2) was deformed 6.3 percent at 345 bars confining pressure. The greatest load was vertical. Note that there are very few fragments between grains. (Compare with Figures 7a and 8a.)



NOT REPRODUCIBLE

Figure 10. Microfractures resulting from triple load. The inverted "v" fracture configuration is typical of three point loads. The central sphere is 0.6 mm in diameter. This specimen (Experiment number 18 on Table 2) was deformed 13.9 percent at 1 kilobar confining pressure. The greatest load was vertical. Note the numerous grain fragments between spheres.



NOT REPRODUCIBLE

Figure 11. Microfractures resulting from four or more loads. This fracture pattern is probably the result of four contacts in and nearly in the plane of section and a fifth contact above or below that plane. The fracture pattern is like that expected for hexagonal packing subjected to  $P_1 \gg P_2$  (Figure 8d). The central sphere is 0.6 mm in diameter. This specimen (Experiment number 5 on Table 2) was deformed 6 percent at 345 bars confining pressure. The greatest load was applied in the vertical direction. (Compare with Figure 8d.)



NOT REPRODUCIBLE

Figure 12. Peripheral microfractures. This sort of peripheral fracture pattern with an essentially undeformed center is expected for hexagonal packing in which a grain is loaded critically at six or more contacts. The central sphere is 0.3 mm in diameter. This specimen (Experiment number 6 on Table 2) was shortened 6.5 percent at 345 bars confining pressure. The greatest load was applied in a vertical direction (compare with Figure 8). Note that some major trends exist especially the trends at about 10 degrees to 20 degrees from vertical on the right hand side of the grain.

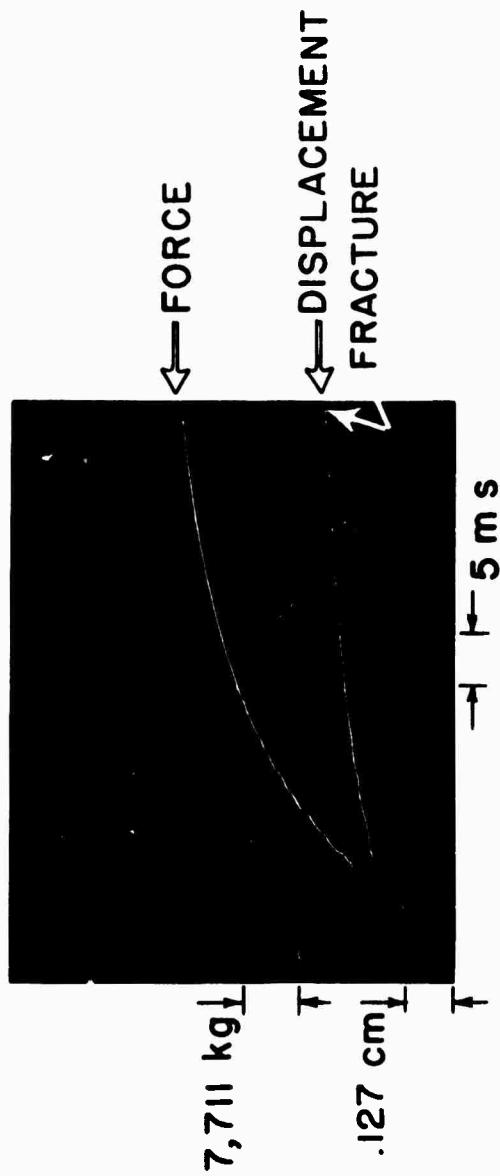


NOT REPRODUCIBLE

Figure 13. Intense microfracturing. At high confining pressure and high strain, pores are filled with fragments, most contacts are broad, and fracture zones tend to be wide. The greatest load was applied vertically. The central sphere is 0.6 mm in diameter. These spheres are in specimen 18 (Table 2).



Figure 14. Chain of microfractures. Fractures commonly connect at grain contacts. The central sphere is 0.3 mm diameter. These spheres are in specimen 6 (Table 2). The greatest load was applied in the vertical direction.



## WESTERLY GRANITE

Figure 15. A typical record of force and displacement versus time for Westerly granite deformed at 1 kb confining pressure. Note almost linear displacement rate of 2.76 cm/sec. The average calculated strain rate is  $6.9 \times 10^{-1}/\text{sec}$ . Failure of the specimen is marked by loss of force and a rapid acceleration of the displacement rate.

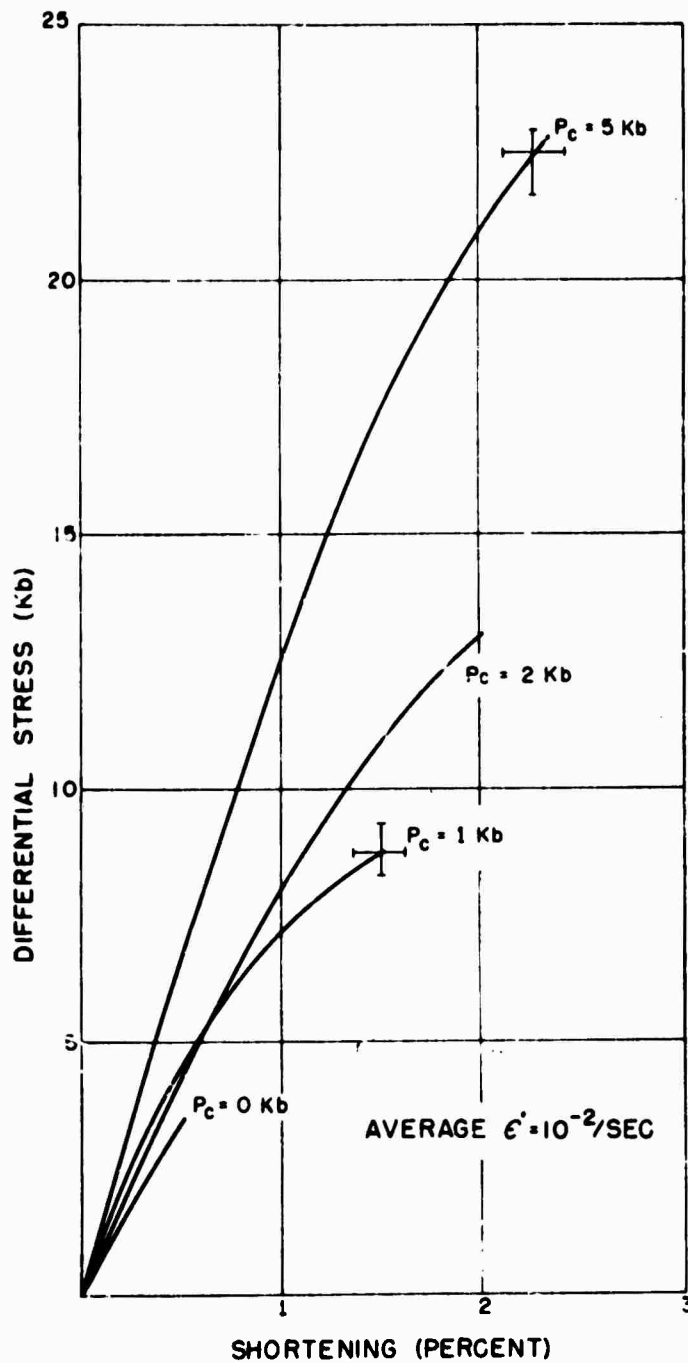


Figure 16. Stress-shortening curves for Westerly granite at an average strain rate of  $10^{-2}/\text{sec}$ . Confining pressures are given for each set of tests.

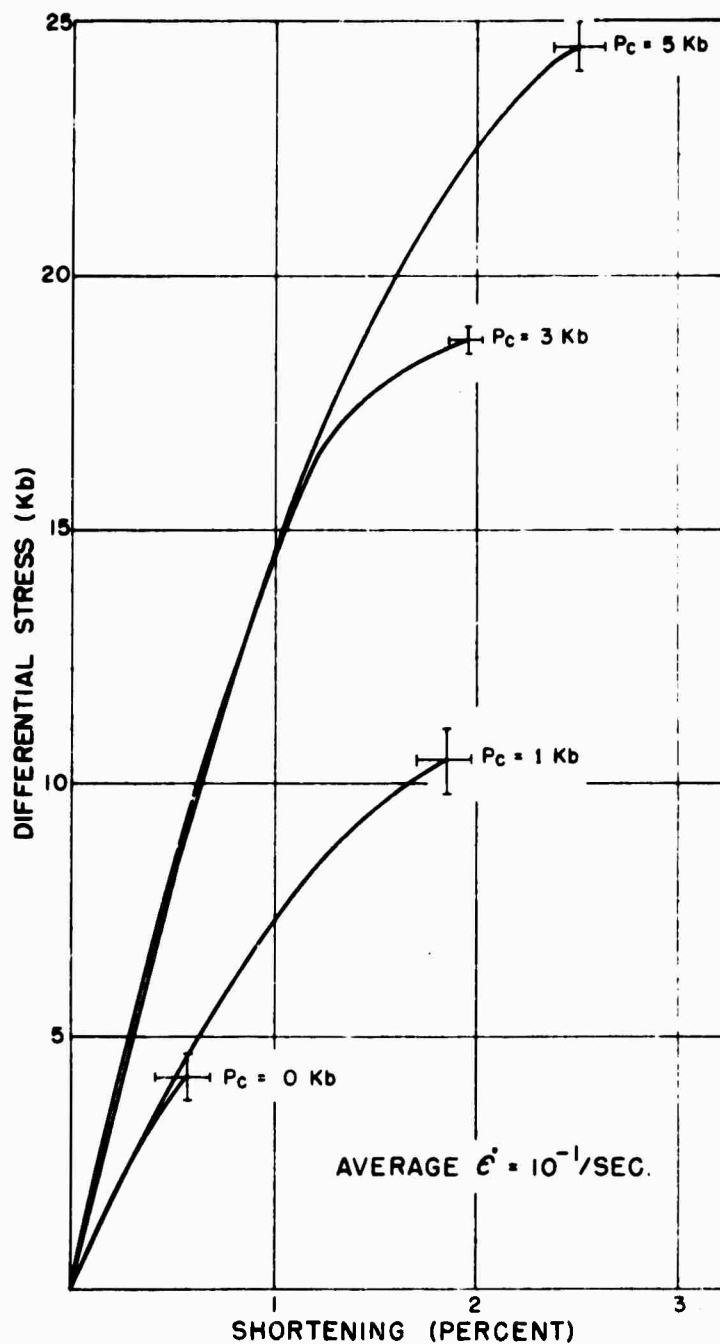


Figure 17. Stress-shortening curves for Westerly granite at an average strain rate of  $10^{-1}/\text{sec}$ . Confining pressures are given for each set of tests.

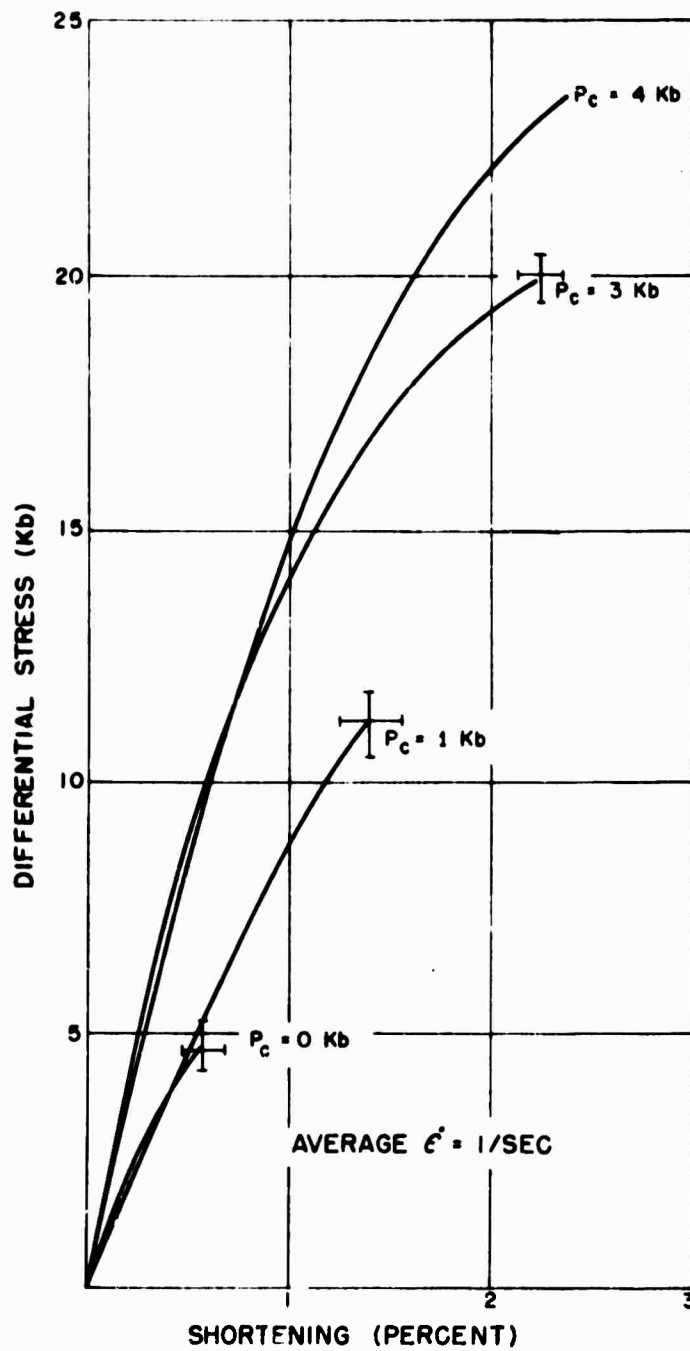


Figure 18. Stress-shortening curves for Westerly granite at an average strain rate of 1/sec. Confining pressures are given for each set of tests.

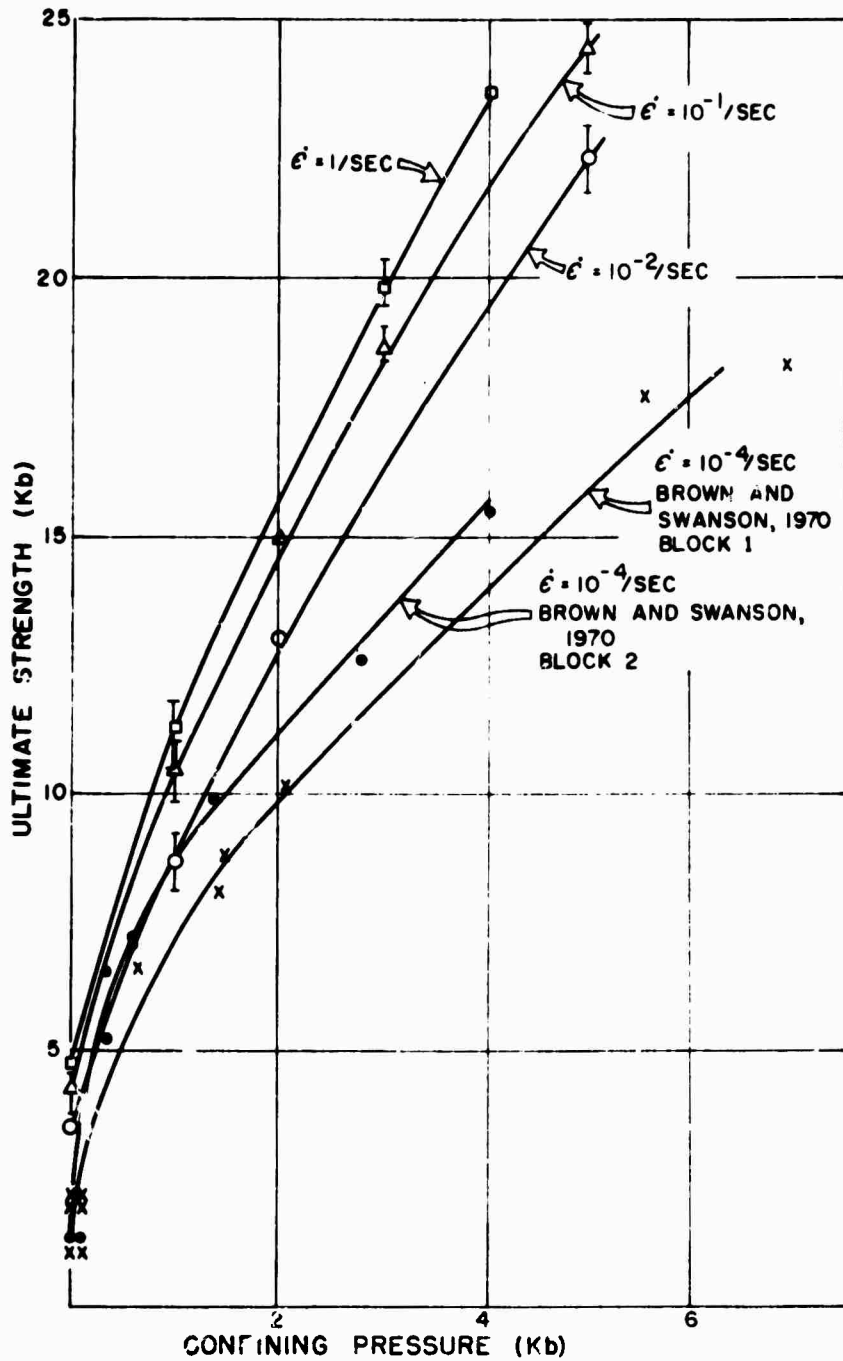


Figure 19. Ultimate strength versus confining pressure for Westerly granite, at strain rates of  $10^{-2}$  to  $1/\text{sec}$ . Data at a strain rate of  $10^{-4}/\text{sec}$  is from Brown and Swanson (1970).

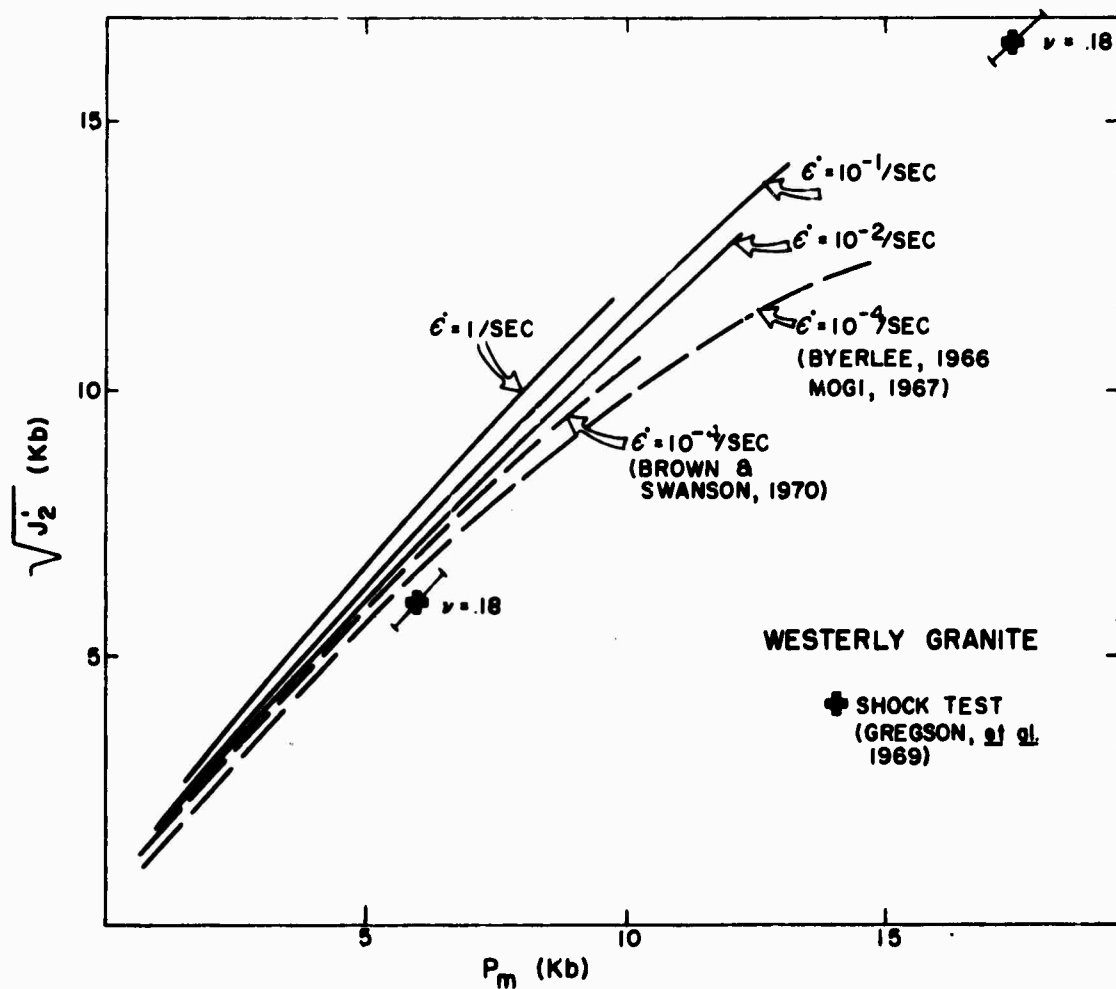


Figure 20. The square root of the second deviatoric stress invariant versus mean pressure for Westerly granite for strain rates of  $10^{-2}$  to 1/sec. Data at a strain rate of  $10^{-4}/\text{sec}$  and shock data are from the sources noted.



NOT REPRODUCIBLE

## SOLENHOFEN LIMESTONE

Figure 21. A typical record of force and displacement versus time for Solenhofen limestone deformed at 1 kb confining pressure. An average displacement rate of 7.34 cm/sec was attained before the yield point was reached. After the onset of permanent shortening an average displacement rate of 50.8 cm/sec and an average strain rate of 12.1/sec was recorded.

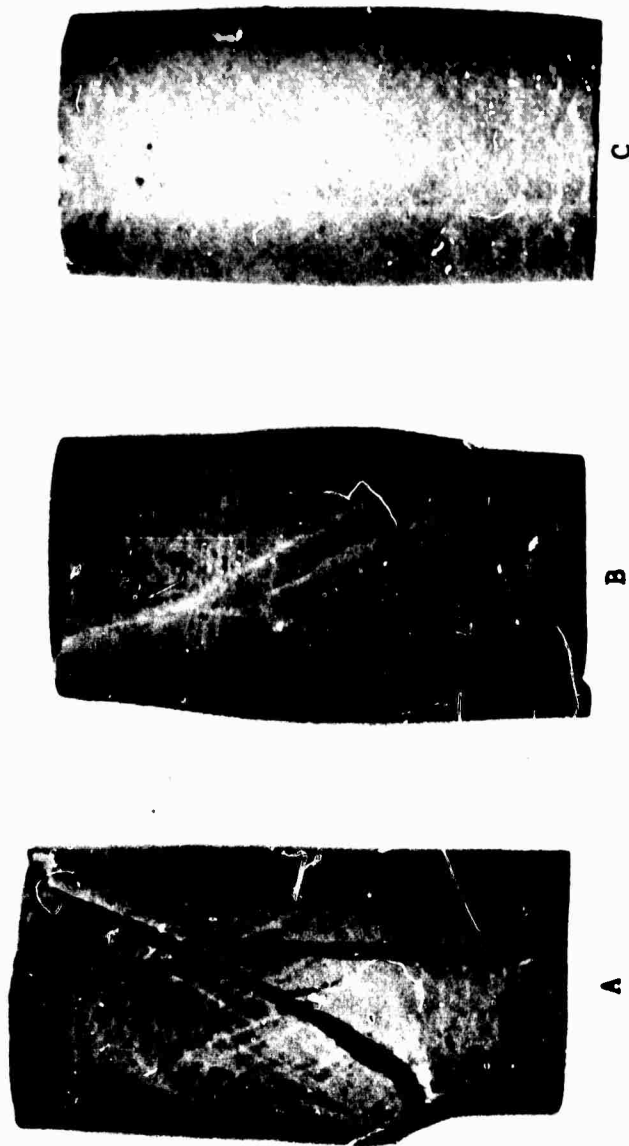


Figure 22. Specimens of Solenhofen limestone illustrating the brittle to ductile transition with increasing confining pressure. All specimens were deformed at an average strain rate of  $10^{-2}$ /sec. Specimens A, B, C were deformed at .5 kb, 1 kb and 2 kb confining pressure respectively.

NOT REPRODUCIBLE

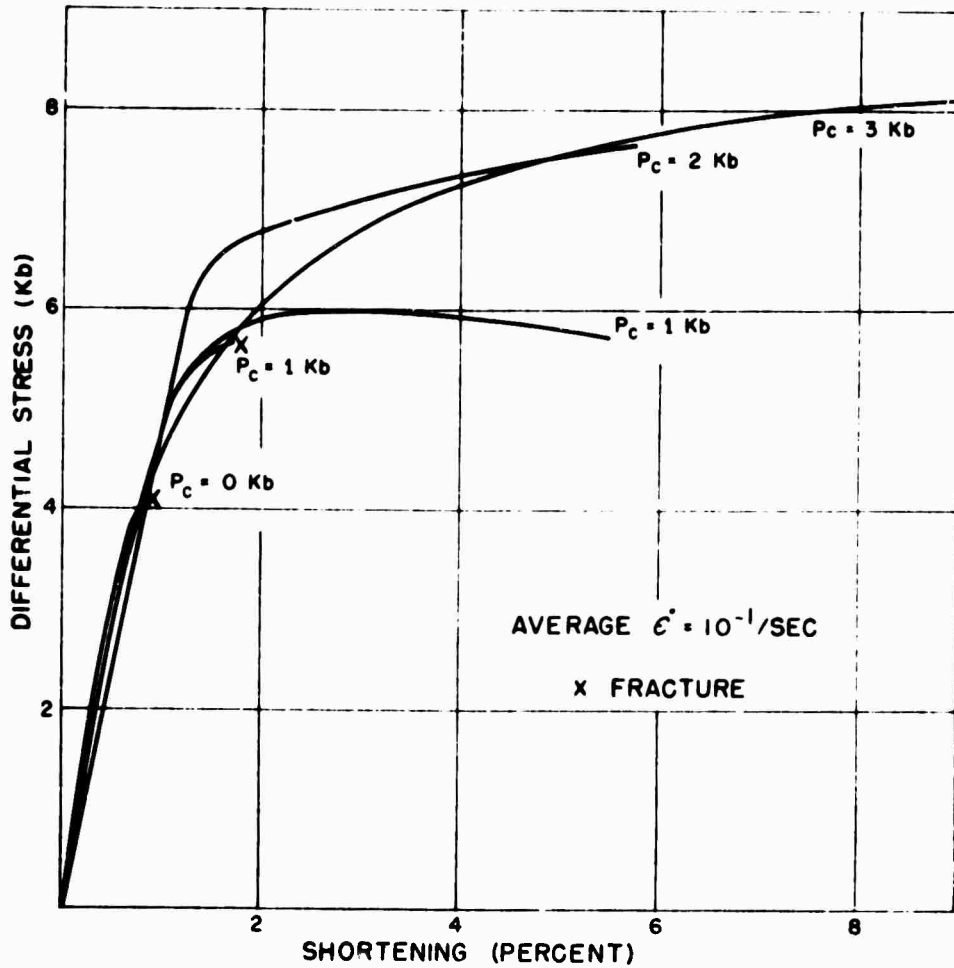


Figure 23. Stress-shortening curves for Solenhofen limestone at an average strain rate of  $10^{-1}/\text{sec}$ . Confining pressures are given for each set of tests.